Direct molecular dynamics simulation of liquid-solid phase equilibria for two-component plasmas

A. S. Schneider,* J. Hughto,† and C. J. Horowitz‡
Department of Physics and Nuclear Theory Center, Indiana University, Bloomington, Indiana 47405, USA

D. K. Berry
University Information Technology Services, Indiana University, Bloomington, Indiana 47408, USA
(Received 17 August 2011; revised manuscript received 18 May 2012; published 20 June 2012)

We determine the liquid-solid phase diagram for carbon-oxygen and oxygen-selenium plasma mixtures using two-phase molecular dynamics simulations. We identify liquid, solid, and interface regions using a bond angle metric. To study finite-size effects, we perform 27 648- and 55 296-ion simulations. To help monitor nonequilibrium effects, we calculate diffusion constants D_i. For the carbon-oxygen system we find that D_{O} for oxygen ions in the solid is much smaller than D_{C} for carbon ions and that both diffusion constants are 80 or more times smaller than diffusion constants in the liquid phase. There is excellent agreement between our carbon-oxygen phase diagram and that predicted by Medin and Cumming. This suggests that errors from finite-size and nonequilibrium effects are small and that the carbon-oxygen phase diagram is now accurately known. The oxygen-selenium system is a simple two-component model for more complex rapid proton capture nucleosynthesis ash compositions for an accreting neutron star. Diffusion of oxygen, in a predominantly selenium crystal, is remarkably fast, comparable to diffusion in the liquid phase. We find a somewhat lower melting temperature for the oxygen-selenium system than that predicted by Medin and Cumming. This is probably because of electron screening effects.

DOI: 10.1103/PhysRevE.85.066405 PACS number(s): 52.65.−y, 97.20.Rp, 64.70.dg

I. INTRODUCTION

Observations of cooling white dwarf (WD) stars provide important information on the ages and evolution of stellar systems [1–4]. The interior of a WD is a Coulomb plasma of ions and a degenerate electron gas. As the star cools this plasma crystallizes. This can delay WD cooling; see, for example, Ref. [5]. Winget *et al*. recently observed effects from the latent heat of crystallization on the luminosity function of WDs in the globular cluster NGC 6397 [6]. Winget *et al*.'s observations may constrain the melting temperature of the carbon and oxygen mixtures expected in these WD cores. In addition, astroseismology provides an alternative way to study crystallization in WD; see, for example, Ref. [7].

Furthermore, material accreting onto a neutron star (NS) will freeze to form new NS crust. A variety of nuclear reactions can take place, including rapid proton capture nucleosynthesis (the rp process [8,9]) followed by electron captures, as the material is advected to higher densities. Horowitz *et al*. studied the crystallization of a complex rp process ash consisting of 17 chemical elements from oxygen to selenium [10]. They found chemical separation upon freezing, with low Z elements preferentially remaining in the liquid NS ocean while high Z elements crystallize to form new NS crust. This change in composition of the ocean may be important for superbursts. These are thought to be energetic thermonuclear explosions of carbon [11–13].

Melting temperatures and other properties of the liquid-solid phase diagram for multicomponent plasmas have been determined from computer simulations. Segretain and Chabrier calculated the carbon-oxygen phase diagram assuming a local density model for the free energy of the solid [14], while, Ogata *et al*. [15,16] and DeWitt *et al*. [17,18] calculated the phase diagram based on Monte Carlo or molecular dynamics (MD) simulation free energies for both the liquid and solid phases. Recently Potekhin *et al*. have made accurate calculations of the free energy of liquid mixtures [19,20] and Medin and Cumming calculated the phase diagram for both binary mixtures such as carbon and oxygen and much more complicated multicomponent mixtures [21].

All of these works determine liquid-solid phase equilibria by equating liquid and solid free energies that have been calculated separately. This procedure allows the use of smaller Monte Carlo or MD simulations where only a single phase is present at a time. However, it may be very sensitive to any small errors in the free energy difference between liquid and solid phases. Indeed for the carbon-oxygen system, Segretain and Chabrier predict higher melting temperatures and a spindle-type phase diagram, while both Ogata *et al*. and Medin and Cumming predict lower melting temperatures and an azeotrope-type phase diagram. In a spindle-type phase diagram the melting temperature of the mixture is always greater than the melting temperature of pure carbon, while in an azeotrope-type phase diagram the melting temperature of the mixture can be lower than that of pure carbon. This difference in phase diagrams could be due to small errors in Segretain and Chabrier's solid free energies.

Furthermore, equating the free energies of liquid and solid phases provides no information on the dynamics of the phase transition. For example, although there have been some studies of nucleation for one-component plasma systems [22,23], there have been almost no studies of nucleation for multicomponent plasmas. Finally, interface properties are not addressed. For one-component systems there has been some

*andschn@umail.iu.edu
†jhughto@astro.indiana.edu
‡horowit@indiana.edu

work on surface properties; see, for example, Ref. [24,25]. For multicomponent systems there is, in general, a gradient in composition across the liquid-solid interface. However, the spatial extent of this gradient has not been determined.

Recently, we performed direct two-phase molecular dynamics simulations of liquid-solid phase equilibria both for carbon-oxygen mixtures in WDs [26] and for a complex 17-component mixture modeling the crust of an accreting neutron star [10]. These simulations have both liquid and solid phases present simultaneously. This allows a direct determination of the melting temperature, and the composition of the liquid and solid phases from a single simulation. Furthermore, phase equilibria for very complicated systems can be simulated in this way.

However, direct simulations need to address potential systematic errors from finite-size effects and from the lack of thermodynamic equilibration. Finite-size effects are potentially important because one must fit not only liquid and solid phases but also two liquid-solid interfaces within the simulation volume. This, in general, requires a larger simulation volume than for simulations of only a single phase. However, recent computer advances have dramatically reduced the computational limitations on these larger simulations. It is now "easy" to simulate much larger systems than have typically been run in the past.

One must run these two-phase simulations long enough to ensure that the phases have come into thermodynamic equilibrium. This may require impurities to diffuse throughout the solid phase. However, diffusion in the solid phase is relatively fast, for these Coulomb systems, because the ions do not have hard core interactions. There is only a relatively soft $1/r$ interaction between ions. As a result, ions can move past one another. We have studied diffusion in Coulomb crystals in a recent paper [27]. If finite-size and nonequilibrium effects are addressed, direct two-phase simulations should yield accurate results. The systematic errors from two-phase simulations are likely very different from previous free energy calculations. Therefore, comparing the two methods provides an important check on both approaches.

In the laboratory, one can observe complex (or dusty) plasma crystals. Complex plasmas are low-temperature plasmas containing charged microparticles; for a review, see Fortov *et al.* [28]. Often the microparticles are micrometer-sized spheres that acquire large electric charges and the strong Coulomb interactions between microparticles can lead to crystallization. Indeed, two-dimensional plasma crystals were first observed in the laboratory in 1994 [29]. Three-dimensional plasma crystals can be studied under microgravity conditions; see, for example, Ref. [30]. Alternatively, one can study systems of charged colloidal spheres. For example, Lorenz and Palberg observed melting and freezing lines for a binary mixture of colloidal spheres [31].

In this paper we study freezing of binary mixtures of carbon and oxygen as well as of oxygen and selenium. The carbon-oxygen system is important for white dwarfs while the oxygen-selenium system provides a simple binary model of the complex rp ash composition in accreting NSs. We perform MD simulations with both 27 648 and 55 296 ions. This allows us to study finite-size effects. We discuss our MD formalism in Sec. II, present results in Sec. III for the carbon-oxygen, and Sec. IV for the oxygen-selenium system, and conclude in Sec. V.

II. FORMALISM

In Sec. II A we describe our two-phase MD simulation formalism. This is very similar to what we used earlier for the freezing of rapid proton capture nucleosynthesis ash on accreting neutron stars [10] and for carbon and oxygen mixtures in WDs [26]. Next, in Sec. II B, we describe our analysis procedure for determining if a given region of the simulation is in a liquid or solid phase.

A. MD formalism

We consider a system of ions, of two different charges, and electrons. The electrons are assumed to form a degenerate Fermi gas. The ions are fully pressure ionized and interact with each other via screened Coulomb interactions. The potential between the ith and jth ion is assumed to be

$$v_{ij}(r) = \frac{Z_i Z_j e^2}{r} e^{-r/\lambda}. \tag{1}$$

Here the ion charges are Z_i and Z_j, r is their separation, and the electron screening length is λ. For cold relativistic electrons, the Thomas-Fermi screening length is $\lambda^{-1} = 2\alpha^{1/2} k_F/\pi^{1/2}$ where the electron Fermi momentum k_F is $k_F = (3\pi^2 n_e)^{1/3}$ and α is the fine structure constant. Finally, the electron density n_e is equal to the ion charge density, $n_e = \langle Z\rangle n$, where n is the ion density and $\langle Z\rangle$ is the average charge.

We cut off the potential for $r > r_{\rm cut} = 8\lambda$. We note that this is a relatively large distance. For example, for a pure carbon system this corresponds to $r_{\rm cut} \approx 24a$ with a the ion sphere radius $a = (3/4\pi n)^{1/3}$. At this point the potential is only $1.4 \times 10^{-5}\, Z^2 e^2/a$. Our simulations are classical and we have neglected the electron mass (extreme relativistic limit). This is to be consistent with our previous work on neutron stars. However, the electron mass is important at the lower densities in WDs and this may change our results slightly [32]. Also quantum effects could play some role at high densities [33,34].

The simulations can be characterized by an average Coulomb parameter Γ,

$$\Gamma = \frac{\langle Z^{5/3}\rangle e^2}{a_e T}. \tag{2}$$

Here $\langle Z^{5/3}\rangle$ is an average over the ion charges, T is the temperature, and the electron sphere radius a_e is $a_e = (3/4\pi n_e)^{1/3}$.

Time can be measured in units of one over the plasma frequency ω_p. Long-wavelength fluctuations in the charge density can undergo oscillations at the plasma frequency. This depends on the ion charge Z and mass M. For mixtures we define a hydrodynamical plasma frequency $\bar{\omega}_p$ from the simple averages of Z and M,

$$\bar{\omega}_p = \left[\frac{4\pi e^2 \langle Z\rangle^2 n}{\langle M\rangle}\right]^{1/2}. \tag{3}$$

Note that other choices for the average over composition in Eq. (3) are possible. However, they are expected to give very similar results for the average plasma frequency.

All of our carbon-oxygen simulations are run for the same electron density of $n_e = 5.026 \times 10^{-4}$ fm^{-3}, while the oxygen-selenium simulations are run for $n_e = 2.254 \times 10^{-3}$ fm^{-3}. Since the pressure is dominated by the electronic contribution, constant electron density corresponds, approximately, to constant pressure. The density can be scaled to any desired value by also changing the temperature T so that the value of Γ [see Eq. (2)] remains the same.

B. Interface-finding algorithm

In this section we describe an algorithm for specifying if a given region of the simulation belongs to the bulk liquid or bulk solid phase or if the region belongs to a liquid-solid interface. Often determining whether a cluster of ions is a liquid or a bcc solid is simple when the cluster is visually inspected. However, this determination is difficult to obtain numerically. For an entire system, phase determination can be accomplished by computing the global order parameter Q_6 [35]; see below. In this work, we use the prescription laid out in Ref. [36] to determine whether individual ions are liquidlike or solidlike.

For each ion i, an ion j is defined as a neighbor if it is within a given radius $r_{\rm cut} = 4a$ with a the ion sphere radius $a = (3/4\pi n)^{1/3}$. The vectors $\hat{\mathbf{r}}_{ij}$ joining neighbors are called bonds. The direction of these vectors can be described by θ_{ij} and ϕ_{ij} in the frame of ion i. The local structure around ion i can be characterized using spherical harmonics $Y_{lm}(\theta_{ij},\phi_{ij})$ by

$$\bar{q}_{lm}(i) = \frac{\sum_{j=1}^{N_b(i)} \alpha(r_{ij}) Y_{lm}(\theta_{ij},\phi_{ij})}{\sum_{i=1}^{N_b(i)} \alpha(r_{ij})}, \tag{4}$$

where $N_b(i)$ is the number of ions bonded with ion i and

$$\alpha(r_{ij}) = \left(\frac{r_{ij} - 4a}{4a}\right)^2 \tag{5}$$

if $r_{ij} < 4a$ and $\alpha(r_{ij}) = 0$ otherwise.

These local order parameters are large in both the solid and the liquid. The global order parameter Q_6 is calculated from an average over all of the N ions,

$$q_{6m} = \frac{1}{N} \sum_{i=1}^{N} \bar{q}_{6m}(i), \tag{6}$$

$$Q_6 = \left[\frac{4\pi}{13} \sum_{m=-6}^{6} q_{6m}^* q_{6m}\right]^{1/2}. \tag{7}$$

This is large in the solid due to the fact that the $\bar{q}_{6m}(i)$ add up coherently. In the liquid, $\bar{q}_{6m}(i)$ add incoherently, so Q_6 is small. This coherence is exploited to determine local order.

For each $\bar{q}_{6m}(i)$ a normalization is applied,

$$\tilde{q}_{6m}(i) \equiv \frac{\bar{q}_{6m}(i)}{\left[\sum_{m=-6}^{6} |\bar{q}_{6m}(i)|^2\right]^{1/2}}. \tag{8}$$

A dot product can now be defined of the vectors $\mathbf{q}_6$ for neighboring particles i and j,

$$\mathbf{q}_6(i) \cdot \mathbf{q}_6(j) \equiv \sum_{m=-6}^{6} \tilde{q}_{6m}(i) \tilde{q}_{6m}^*(j). \tag{9}$$

By construction, $\mathbf{q}_6(i) \cdot \mathbf{q}_6(i) = 1$.

We use the same criterion as Ref. [36] for determining whether two particles are connected, namely, $\mathbf{q}_6(i) \cdot \mathbf{q}_6(j) > 0.5$. This criterion will be met for most of the bonds in the solid. In the liquid, two neighbors may be in phase and considered connected, but that is unlikely to be true for all of the neighbors. Therefore, we use a threshold on the number of connections to determine if an ion is solidlike or liquidlike. This threshold is 20 connections. An ion is considered solidlike if it is connected to 20 or more neighbors. Otherwise the ion is considered liquidlike. Note that on average an ion in the carbon-oxygen system has about 62 neighbors.

Now that each ion is tagged as either solidlike or liquidlike, the interface in our two-phase simulations can be found. Deep in the solid, a vast majority of the ions within a certain radius of a given ion are identified as solidlike. In the bulk of the liquid a similar majority is identified as liquidlike. Along the interface, there is a mixture of solidlike and liquidlike ions. For this reason, we tag an ion as being in the solid or liquid if a large majority (>80%) of the ions within $4a$ of a given ion are the same phase. If this criterion is not met, then the ion is determined to be in the interface. Performing this identification leads to results that will be shown in Fig. 2 of Sec. III. Notice that ions determined to be in the interface are found where one would expect them, along the border of the solid and liquid phases.

Note that this procedure is slightly modified for the oxygen-selenium system. Bonds involving oxygen ions, in a predominantly selenium crystal, are not as well ordered as selenium-selenium bonds. Therefore, for this system we consider only selenium-selenium bonds, as discussed in Sec. IV.

III. RESULTS FOR THE CARBON AND OXYGEN SYSTEM

In this section we present results for the phase diagram and diffusion constants for carbon and oxygen systems. Our previous carbon and oxygen results in Ref. [26] were based on MD simulations with 27 648 ions. Here we perform three larger simulations with 55 296 ions in order to study finite-size effects. In addition we calculate diffusion constants in order to monitor nonequilibrium effects.

To minimize finite-size effects, we use a rectangular simulation volume that is twice as long in the z direction compared to the x and y directions. We use periodic boundary conditions in this rectangular box. Note that we evaluate the interaction between two particles as the single interaction with the nearest periodic image. We do not include an Ewald sum over further periodic images because our box is so large that interactions with periodic images other than the nearest one are very small. The initial conditions consist of a cube of crystalline phase that is stacked together in the z direction with an equal-sized cube of liquid phase. This rectangular geometry increases the distance between the two liquid-solid interfaces compared to a cubical simulation volume.

A. Run with 75% oxygen

Our first simulation has an average composition of 75% oxygen and 25% carbon (by number). We independently prepare solid and liquid initial conditions and then combine

them to obtain the full 55 296-ion initial conditions. Based on our earlier results suggesting that the solid phase will be enriched in oxygen from [26], we prepare the liquid configuration with 70% oxygen, 30% carbon and the solid configuration with 80% oxygen, 20% carbon. We start with a 3456-ion configuration with random positions and velocities and cool the system until it solidifies. We then combine eight copies of this 3456-ion solid to make a 27 648-ion solid configuration and continue to evolve this 27 648-ion system for a time $t\bar{\omega}_p = 8900$ at $\Gamma = 213.1$. We form a liquid configuration by starting with an independent 3456-ion system with random coordinates and evolve the system for a time $t\bar{\omega}_p = 4400$ at the same Γ. We combine eight copies of this liquid configuration to make a 27 648-ion liquid and evolve for a further $t\bar{\omega}_p = 8800$. Finally we combine the 27 648-ion solid configuration with the 27 648-ion liquid configuration to form the full 55 296-ion initial condition.

This initial condition is not equilibrated for a number of reasons. First the two interfaces between liquid and solid may have high energies because we have simply combined two different initial conditions. There may be liquid and solid ions close to each other. In addition, the solid part of the initial condition may not be equilibrated because it has carbon and oxygen ions positioned on lattice sites more or less at random. The equilibrated solid may have important correlations between ions of different charges. Finally, the compositions of the liquid and solid phases may be wrong. Therefore, carbon ions may diffuse into or out of the solid region until the compositions of the liquid and solid phases equilibrate. This may require evolving the system for a considerable time.

We evolved the full 55 296-ion system for a total time $2.8 \times 10^6/\bar{\omega}_p$ using a velocity Verlet [37] time step of $0.177/\bar{\omega}_p$. We employed a simple hybrid OpenMP/MPI computer code and use about 768 cores on the Cray XT5 system Kraken [38]. This evolution took a total of about 2 weeks. During the run we rescaled the velocities every 100 time steps in order to keep the temperature approximately constant. We slowly adjust the temperature so that approximately half of the system remains liquid and half solid. In Fig. 1 we show the final configuration of the 55 296 ions. The bottom half of the simulation volume is seen to contain a crystalline region. We use the procedure of Sec. II B to determine which parts of the system are liquid, solid, or belong to the two liquid-solid interfaces. This is shown in Fig. 2. Note that the interface regions are not rectangular and show some fluctuations.

In Fig. 3 we show the fluctuations in Γ (or equivalently $1/T$) during the run. We calculate the final $\bar{\Gamma}$ value as the average of Γ over the last third of the run; see Table I. We define the scaled fluctuations in Γ as $\delta\Gamma$,

$$\delta\Gamma = \frac{\Gamma - \bar{\Gamma}}{\bar{\Gamma}}. \tag{10}$$

As the run started, it was necessary to use a low temperature (high Γ) in order to keep the badly nonequilibrated solid frozen. However, as the system rapidly equilibrated the temperature could be quickly reduced towards its final equilibrated value. The temperature is then seen to fluctuate around this value at the 0.5% level or less. Figure 3 also shows the fraction of the system that is solid, liquid, or interface vs time. The interface fraction is very constant (since the thickness of the interface depends on our definition in Sec. II B but is time independent). The temperature is adjusted to keep the fraction liquid and fraction solid more or less constant.

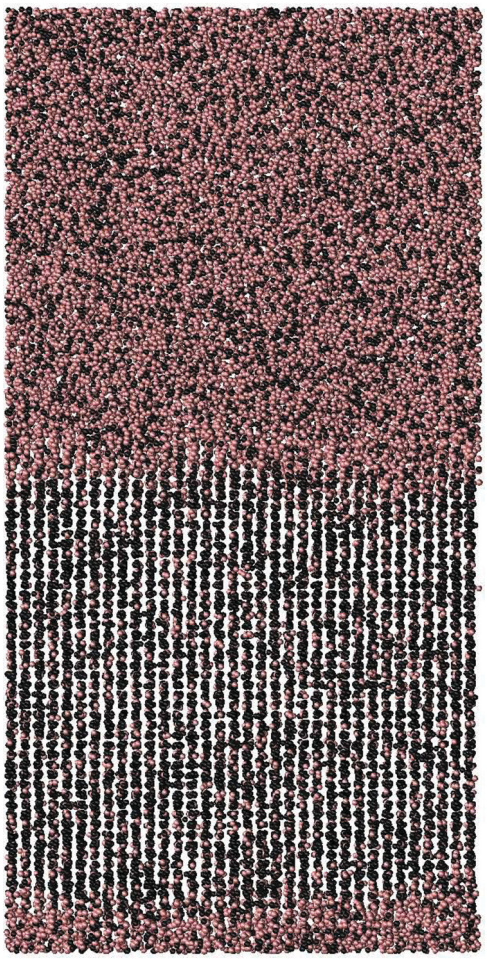

FIG. 1. (Color online) Final configuration of carbon ions (light red) and oxygen ions (black) in a 55 296-ion simulation that consisted of 75% oxygen and 25% carbon.

In Fig. 4 we show the composition (oxygen number fraction x_O) of the solid x_O^s, liquid x_O^l, and interface x_O^i regions as a function of time. The interface composition is seen to remain near the average value $x_O^i \approx 0.75$ while the solid becomes enriched in oxygen so that $x_O^s \approx 0.8$ and the liquid is depleted in oxygen $x_O^l \approx 0.7$. The compositions, averaged over the final third of the run, are collected in Table I.

In Fig. 5 we show the oxygen composition x_O vs position in the simulation volume at the end of the run. We divide up the simulation volume into 50 slices according to the z coordinate, with slice 1 being at the bottom of Fig. 1 and slice 50 being at the top. For reference we show in Fig. 5 the fraction of ions in a given slice that are in the solid, liquid, and interface regions. For example, we see that slices 6 to 21 are all solid. We note that there are some fluctuations in the composition of the solid region, as a function of position, and there are gradients in composition across the interface regions.

We calculated diffusion constants using the methods of Ref. [27] in order to check on equilibration. Figure 5 shows

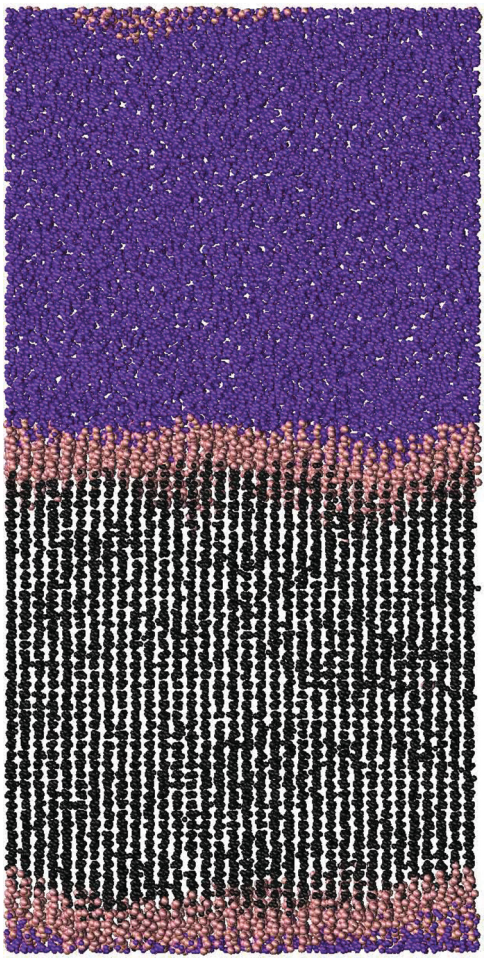

FIG. 2. (Color online) Final configuration of liquid (dark purple), interface (light red), and solid (black in bottom half) ions from a 55 296-ion simulation that consisted of 75% oxygen and 25% carbon. These liquid, solid, and interface, regions are determined using a bond angle metric as discussed in Sec. II B.

diffusion constants compared to a reference value D_0,

$$D_0 = \frac{3\bar{\omega}_p a^2}{\Gamma^{4/3}}, \tag{11}$$

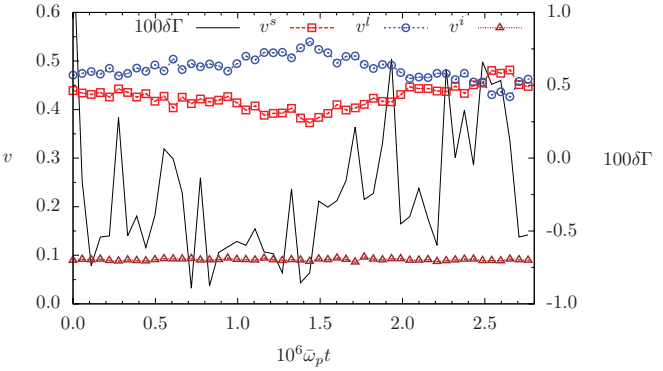

FIG. 3. (Color online) Fractional fluctuations in the Coulomb parameter, $\delta\Gamma$ (solid black line and right hand scale) [see Eq. (10)], vs simulation time t for a 55 296-ion system with 75% oxygen and 25% carbon. Also shown are the fractions of the system that are solid (red squares), liquid (blue circles), or interface (brown triangles).

TABLE I. Equilibrium compositions of our 55 296-ion runs. The oxygen number fraction of the whole system is x_O; the Coulomb parameter averaged over the last third of the run $\bar{\Gamma}$ (determined from the final temperature and x_O). The composition of the solid is x_O^s, that of the liquid is x_O^l, and that of the interface regions is x_O^i. Statistical errors in the last digit are quoted in parentheses.

x_O	$\bar{\Gamma}$	x_O^s	x_O^l	x_O^i
0.75	204.5(8)	0.806(1)	0.699(3)	0.740(7)
0.50	221.7(9)	0.552(1)	0.454(3)	0.494(8)
0.25	213.2(7)	0.250(2)	0.249(2)	0.252(6)

for both carbon and oxygen ions at various positions in the simulation volume; see also Table II. Diffusion is seen to be relatively fast in the liquid region with D_C^l for carbon being only slightly larger than D_O^l for oxygen ions. This is consistent with the results of Ref. [39]. In contrast, D_C^s in the solid is almost 100 times smaller than in the liquid. This is similar to the one-component solid diffusion results of Ref. [27]. Furthermore, in the solid, D_O^s is much smaller than D_C^s. The composition of the solid can equilibrate by carbon ions diffusing in to reduce x_O^s or diffusing out to increase x_O^s. One may not need to wait for the oxygen ions to diffuse throughout the solid. Therefore, we expect the equilibration time of our system to be determined by D_C^s in the solid instead of the smaller D_O^s. We find that diffusion is isotropic in the interior of the liquid and solid regions and somewhat nonisotropic near the interfaces.

B. Run with 50% oxygen

Our second 55 296-ion run has an overall composition of 50% oxygen and 50% carbon. We started it in a very similar manner as for the 75% oxygen run except that the initial composition of the solid was assumed to be 55% oxygen, while the liquid was assumed to be 45% oxygen. This is based on our earlier results [26]. Figure 6 shows the fluctuations in Γ, and the fractions of the system that are liquid, solid, and interface as a function of time. The compositions of these regions vs time are shown in Fig. 7 and the compositions averaged over

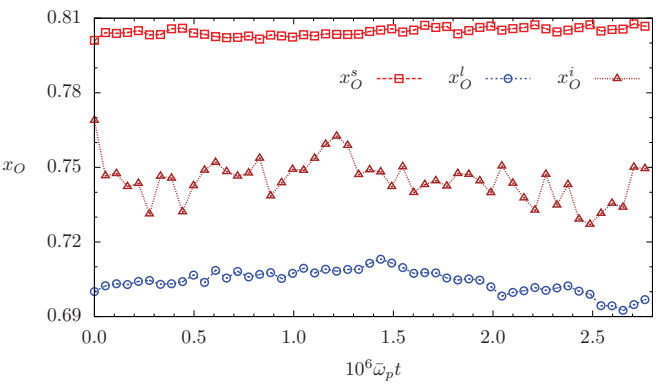

FIG. 4. (Color online) Number fractions of oxygen vs simulation time for liquid x_O^l (blue circles), solid x_O^s (red squares), and interface x_O^i (brown triangles) regions. This is for a 55 296-ion simulation that is overall 75% oxygen and 25% carbon.

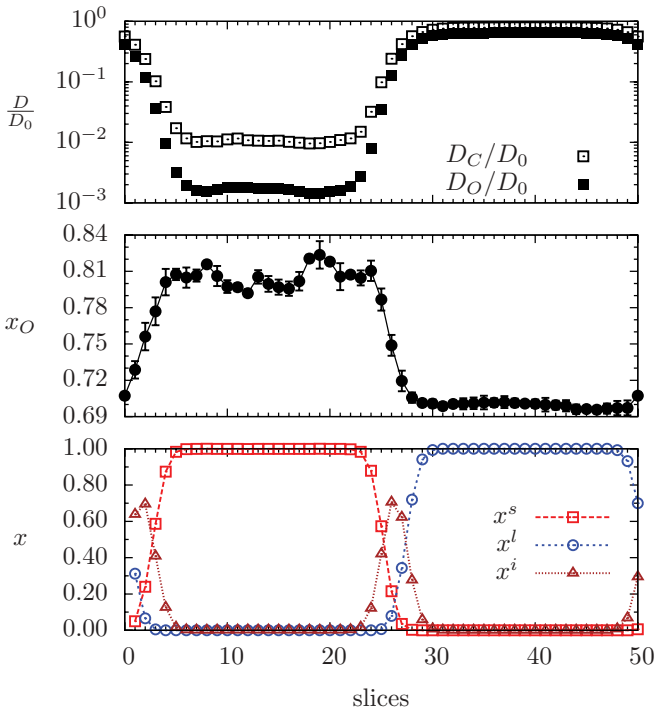

FIG. 5. (Color online) Number fractions of oxygen x_O for different slices (or regions, see text) of the simulation volume (middle panel). Also shown in the top panel are diffusion constants D for carbon ions (open squares) and for oxygen ions (filled squares). Finally the bottom panel shows the fraction of ions that are solid (squares), liquid (circles), or interface (triangles). This is averaged over the last third of the run of the 55 296-ion simulation that is overall 75% oxygen and 25% carbon.

the final third of the run are collected in Table I. We note that there is very little time dependence to these compositions.

In Fig. 8 we show composition vs position. Again there are some fluctuations in the composition of the solid. Diffusion constants D are collected in Table II. In general D as a function of position is very similar to our results from the 75% oxygen simulation. However, we note that D in the solid is somewhat smaller than for the 75% oxygen run.

C. Run with 25% oxygen

Our final 55 296-ion run has an overall composition of 25% oxygen and 75% carbon. We started it in a very similar manner as for the 75% oxygen run except that the initial composition of the solid was assumed to be equal to that of the liquid, with

TABLE II. Diffusion coefficients of liquid and solid phases averaged over the last third of the runs. Results are expressed as D_X^p in units of D_0. The letter p denotes the phase, s for solid and l for liquid, while X stands for the ion species, C for carbon and O for oxygen. Statistical errors in the last digit are quoted in parentheses.

x_O	D_C^l	D_O^l	D_C^s	D_O^s
0.75	0.80(1)	0.64(1)	0.011(3)	0.0017(1)
0.50	0.67(1)	0.55(1)	0.0070(4)	0.0012(1)
0.25	0.64(1)	0.52(1)	0.0031(2)	0.0007(1)

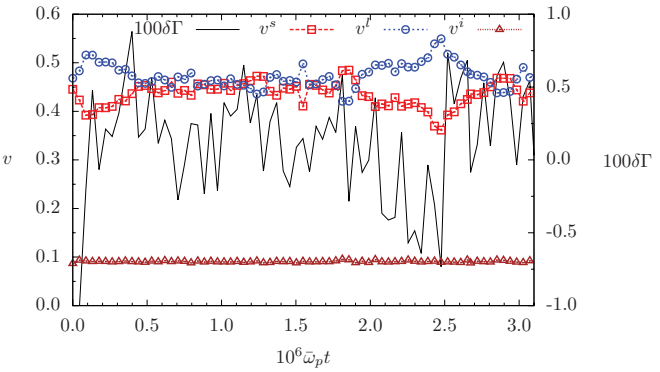

FIG. 6. (Color online) Fractional fluctuations in Coulomb parameter, $\delta\Gamma$ (solid black line and right hand scale) [see Eq. (10)], vs simulation time t for a 55 296-ion system with 50% oxygen and 50% carbon. Also shown are the fractions of the system that are solid (red squares), liquid (blue circles), or interface (brown triangles).

both at 25% oxygen. This is because our earlier simulations found only small chemical separation [26]. Figure 9 shows the fluctuations in Γ, and the fractions of the system that are liquid, solid, and interface as a function of time. The compositions of these regions vs time are shown in Fig. 10 and the compositions averaged over the final third of the run are collected in Table I. We note that all compositions are near 25% oxygen. However, there is a small tendency for the interface regions to be slightly enriched in oxygen compared to both the liquid and solid regions. Note that the fluctuations in the interface composition are larger than the fluctuations in the compositions of the liquid and solid regions because the interface contains fewer ions. The composition of the liquid is very close to that of the solid although, at some times, there are small fluctuations in these compositions. Of course in the thermodynamic limit the composition of the interface is not relevant. Nevertheless, our MD simulation could be showing a real effect where the interface is enriched in oxygen even if the liquid and solid have nearly equal compositions.

In Fig. 11 we show composition vs position. The composition is nearly constant independent of position. However, again there are some fluctuations in the composition of the solid. Diffusion constants D are collected in Table II. Now D

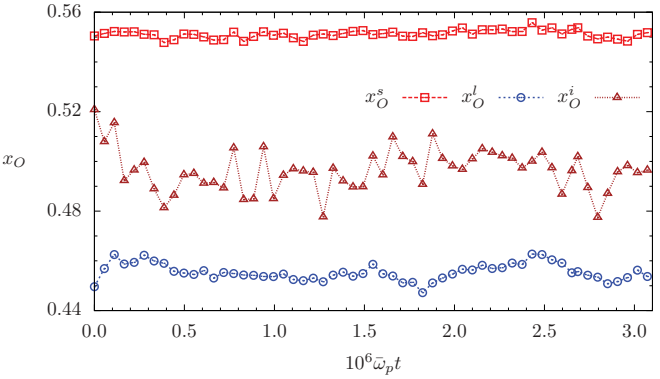

FIG. 7. (Color online) Number fractions of oxygen vs simulation time for liquid x_O^l (blue circles), solid x_O^s (red squares), and interface x_O^i (brown triangles) regions. This is for a 55 296-ion simulation that is overall 50% oxygen and 50% carbon.

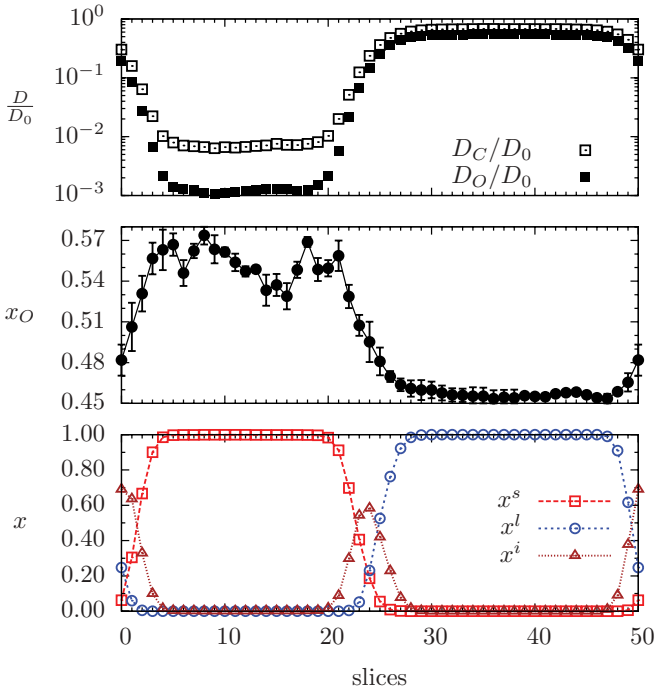

FIG. 8. (Color online) Number fractions of oxygen x_O for different slices (or regions, see text) of the simulation volume (middle panel). Also shown in the top panel are diffusion constants D for carbon ions (open squares) and for oxygen ions (filled squares). Finally the bottom panel shows the fraction of ions that are solid (squares), liquid (circles), or interface (triangles). This is averaged over the last third of the run of the 55 296-ion simulation that is overall 50% oxygen and 50% carbon.

in the solid, for both carbon and oxygen, is smaller than in the 75% or 50% oxygen runs.

D. Carbon-oxygen phase diagram

We now present the liquid-solid phase diagram implied by the simulations in Secs. III A, III B, and III C. Figure 12 shows the phase diagram as a function of x_O. The y axis is the melting temperature T divided by the melting temperature T_C

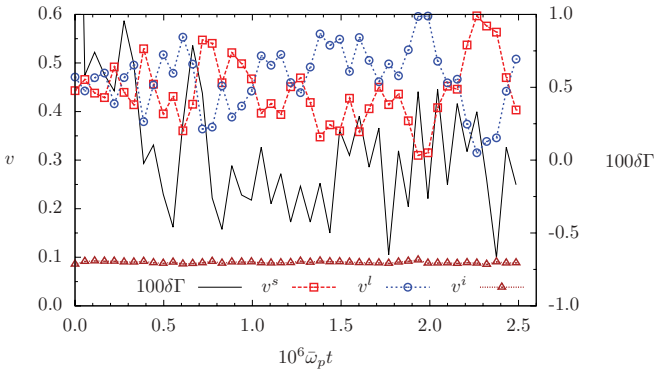

FIG. 9. (Color online) Fractional fluctuations in Coulomb parameter, $\delta\Gamma$ (solid black line and right hand scale) [see Eq. (10)], vs simulation time t for a 55 296-ion system with 25% oxygen and 75% carbon. Also shown are the fractions of the system that are solid (red squares), liquid (blue circles), or interface (brown triangles).

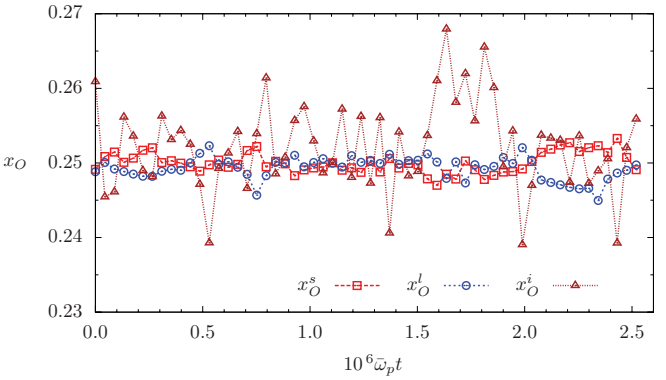

FIG. 10. (Color online) Number fractions of oxygen vs simulation time for liquid x_O^l (blue circles), solid x_O^s (red squares), and interface x_O^i (brown triangles) regions. This is for a 55 296-ion simulation that is overall 25% oxygen and 75% carbon.

for pure carbon. We assume the pure carbon system melts at $\Gamma_m = 178.4$ [26]. This differs slightly from the one-component plasma result because we include the effects of electron screening.

The points plotted in Fig. 12 are listed in Table I. Overall our 55 296-ion results are close to our previous results that used 27 648-ion simulations [26]. However, there are some noticeable differences. The 25% oxygen simulation with 55 296 ions has nearly equal liquid and solid compositions,

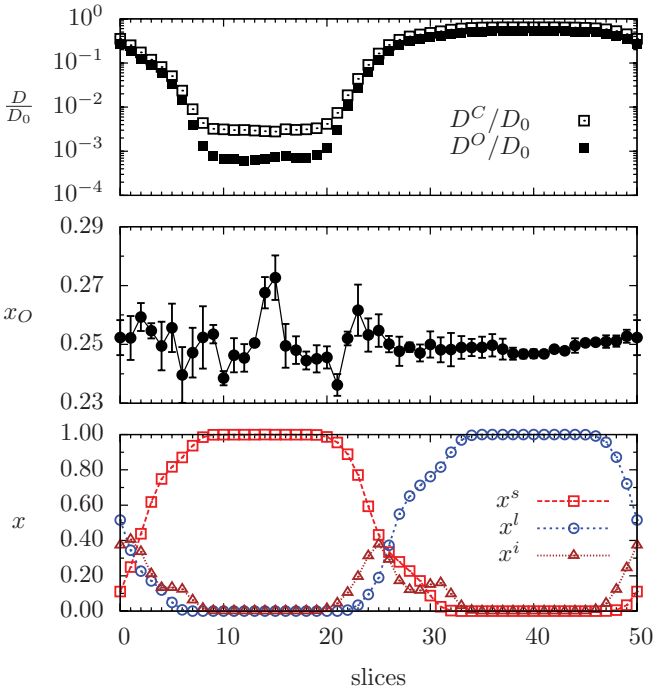

FIG. 11. (Color online) Number fractions of oxygen x_O for different slices (or regions, see text) of the simulation volume (middle panel). Also shown in the top panel are diffusion constants D for carbon ions (open squares) and for oxygen ions (filled squares). Finally the bottom panel shows the fraction of ions that are solid (squares), liquid (circles), or interface (triangles). This is averaged over the last third of the run of the 55 296-ion simulation that is overall 25% oxygen and 75% carbon.

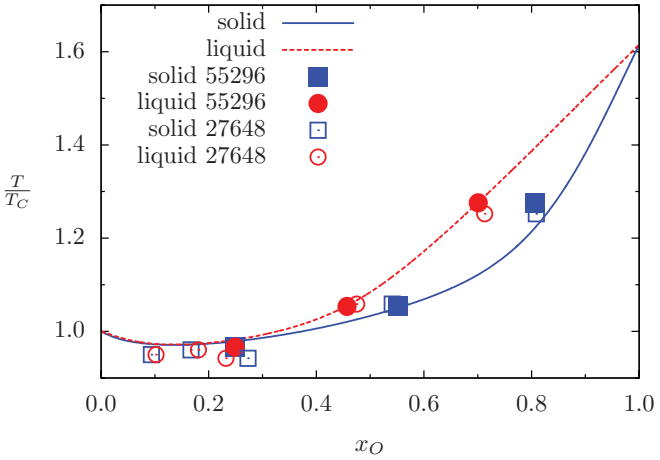

FIG. 12. (Color online) Carbon-oxygen phase diagram plotting the composition of the liquid phase (upper red curve or circles) that is in equilibrium with the solid phase (lower blue curve or squares). Our present results from 55 296-ion simulations are filled symbols while the open symbols are our previous results with 27 648 ions from Ref. [26]. The curves are the results of Medin and Cumming [21].

while the previous 27 648-ion simulation found the solid slightly enriched in oxygen and found a slightly lower melting temperature. The 50% oxygen simulation with 55 296 ions has a slightly larger difference in composition between the liquid and solid than previous 27 648-ion simulations. Finally the 75% oxygen simulation with 55 296 ions has a slightly higher melting temperature than the previous 27 648-ion result. This suggests that finite-size effects, while not zero for the 27 648-ion simulations, are relatively small.

The agreement between our 55 296-ion results and the model of Medin and Cumming is excellent. All three liquid compositions, and two of the three solid compositions, from Table I are very close to Medin and Cumming's results. The only small difference is that our solid composition from the 75% oxygen simulation is not quite as oxygen rich as that of Medin and Cumming. This one difference could be due to a small remaining systematic error in our simulation, or to a small error in the model liquid and solid free energies used by Medin and Cumming. In any case, the small finite-size corrections in going from 27 648-ion to 55 296-ion simulations improve the agreement between our MD simulations and Medin and Cumming's results.

What are the nature of the errors from finite-size and/or nonequilibrium effects? Although small, the errors appear to go in different directions for our three simulations. For the 25% oxygen run the 55 296-ion simulation has a higher melting temperature and much smaller difference between the composition of the liquid and solid compared to 27 648-ion results. This is in a region of the phase diagram where the melting temperature is almost independent of composition. Therefore the equilibrium compositions may be very sensitive to any small errors.

For 50% oxygen, the 55 296-ion simulation has a larger difference between the compositions of the liquid and solid compared to 27 648-ion results. Perhaps the simplest finite-size effect would arise if the composition gradient across an interface extended over a distance comparable to the box size. In this case simulations with small boxes might have more nearly equal liquid and solid compositions than simulations with larger boxes. For example, in Fig. 9 the gradient in composition extends over a distance up to perhaps as many as 10 slices and the distance between the two liquid-solid interfaces is 25 slices. In contrast, the 27 648-ion runs from Ref. [26] are in a cubical box where the distance between the two liquid-solid interfaces is a factor of 2 smaller (equivalent to of order 12.5 slices). Thus, there could be some small finite-size effects for 27 648-ion runs.

Finally, there could be a statistical component to the errors coming from a variety of nonequilibrium effects. For example, fluctuations in the location of an interface could create a new solid region and the composition of this region might not have time to equilibrate. Alternatively there could be composition changes from large fluctuations. One could test for a variety of errors of this type by simply repeating these simulations a number of times with different initial conditions. Unfortunately, we have not had time to do this for the present paper. However, we plan to do this in the future.

The good agreement between our phase diagram and that of Medin and Cumming strongly suggests that the remaining errors in our direct MD simulation approach are small. And, in addition, it suggests that the model free energies employed by Medin and Cumming are good, at least for the carbon-oxygen system. Furthermore, *we conclude that the phase diagram for the carbon-oxygen system may be accurately known*. We emphasize that our direct MD simulations only work at all because diffusion in the solid phase is relatively fast [27]. Had diffusion been slow then it would be very difficult to equilibrate the solid phases.

We find that direct two-phase MD simulations can accurately determine liquid-solid phase equilibria. This result is very useful because direct MD simulation can be applied to many other systems, including very complex ones. Furthermore, direct MD simulations for a few compositions may provide very helpful benchmarks for simpler models. Note that simulations with a somewhat large number of particles may be necessary and these may have to be run for extended simulation times. However, rapid advances in computer power should make such simulations even easier in the future.

IV. RESULTS FOR OXYGEN AND SELENIUM SYSTEMS

In this section we present results for the phase diagram and diffusion constants for oxygen and selenium systems. This two-component system has a much larger ratio of charges, and this leads to a very different phase diagram, than for the carbon and oxygen system of Sec. III. We perform MD simulations with both 27 648 and 55 296 ions in order to monitor finite-size effects. In general we present figures for the larger 55 296-ion simulations and then include both 27 648- and 55 296-ion results in tables. These simulations follow closely the formalism of Sec. II and the procedures of Sec. III.

However, the interface-finding algorithm in Sec. II B is slightly modified. The bond angles for oxygen ions can be liquidlike (more random) even in the solid phase. Therefore, we only take into account selenium ions in the bond angle algorithm. By ignoring all oxygen ions in the system we

determine whether a selenium ion is solidlike or liquidlike by analyzing how it bonds to its neighboring selenium ions. As in Sec. II B, ions are considered neighbors if they are within a distance $r_{ij} < 4a$ of each other. Once all selenium ions have been identified as solidlike or liquidlike we tag an ion (oxygen or selenium) as being in the bulk of the solid or liquid if a large majority (>80%) of the selenium ions within $4a$ of it are the same phase. If this criterion is not met, then the ion is determined to be in the interface.

We now discuss runs with 98%, 90%, 80%, 70%, 60%, and 50% selenium and then we will collect results for the oxygen-selenium phase diagram. Although most runs appear to be equilibrated by the end of the simulations, we note that the 60% and 50% selenium runs are not equilibrated after using a reasonable amount of computer time. We discuss this below.

A. Run with 98% selenium

As for the carbon-oxygen systems we prepare solid and liquid initial conditions separately and then combine them to obtain the full 55 296-ion initial conditions. To prepare the solid we start with a 432-ion system that is composed of 98% selenium ions with random positions and velocities. The system is evolved at a temperature close to its expected melting temperature for $t\bar{\omega}_p = 4500$ using a time step of $0.11\bar{\omega}_p$. Due to finite-size effects it solidifies. We then make eight copies of this 432-ion system to obtain a 3456-ion solid and evolved it for $t\bar{\omega}_p \simeq 20\,000$ keeping a time step of $0.11\bar{\omega}_p$. Eight copies of this system are made to obtain a 27 648-ion solid. This solid is evolved for $t\bar{\omega}_p \simeq 20\,000$ with a time step of $0.22\bar{\omega}_p$.

The liquid is prepared in a similar fashion. We start with a 3456-ion system that is 98% selenium ions with random positions and velocities. This system is evolved for $t\bar{\omega}_p \simeq 20\,000$ with a time step of $0.11\bar{\omega}_p$. Eight copies of this system are made to obtain a 27 648-ion liquid which is evolved for $t\bar{\omega}_p \simeq 20\,000$ using a time step of $0.22\bar{\omega}_p$. Finally, we place the 27 648-ion liquid configuration on top of the 27 648-ion solid configuration to form the full 55 296-ion initial conditions.

The temperature was adjusted during the run to keep approximately equal volume fractions of solid and liquid as shown in Fig. 13. The number fractions of selenium $x_{\rm Se}$ in the solid, liquid, and interface are shown in Fig. 14 versus simulation time; see also Table III. These fractions do not change much in the second half of the run, suggesting that the system is (at least approximately) equilibrated.

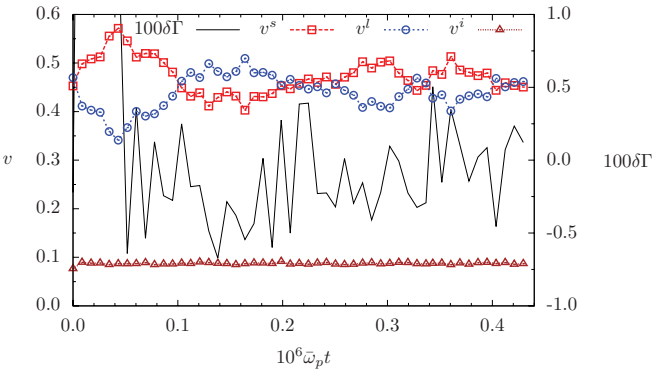

FIG. 13. (Color online) Volume fractions of solid (squares), liquid (circles), and interface (triangles) versus time for a 55 296-ion simulation that is overall 2% oxygen and 98% selenium. Also shown are fluctuations $\delta\Gamma$ in the Coulomb parameter (solid line); see Eq. (10).

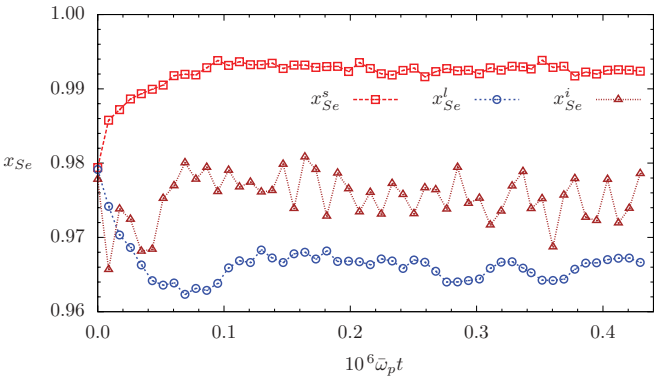

FIG. 14. (Color online) Number fractions of selenium $x_{\rm Se}$ in the solid (squares), liquid (circles), and interface (triangles) versus time for a 55 296-ion simulation that is overall 2% oxygen and 98% selenium.

In Fig. 15, in the middle panel, we show the number fraction of selenium $x_{\rm Se}$ for different slices (regions) of the simulation volume. This is at the end of the simulation. In the solid, $x_{\rm Se}$ is seen to be nearly constant and independent of position. This is consistent with the system having reached equilibration. Diffusion constants D are also shown in Fig. 15 in the top panel and listed in Table IV. For selenium D in the solid is seen to be three orders of magnitude smaller than D in the liquid. However, the behavior is very different for oxygen. Diffusion is nearly the same in the liquid and solid regions. Indeed in the solid, D for oxygen is over three orders of magnitude larger than D for selenium. Presumably the effective size of oxygen ions in the solid (ion sphere radius) is small enough so that the oxygen can diffuse relatively easily through the larger crystal lattice of selenium ions. Note that this behavior for oxygen in a selenium crystal is very different from that for carbon in an oxygen crystal as found in Sec. III; see Fig. 5.

B. Run with 90% selenium

The inital conditions for the 90% selenium simulations were prepared similarly to the 98% ones. The only difference was

TABLE III. Equilibrium compositions of our 55 296-ion runs. The selenium number fraction of the whole system is $x_{\rm Se}$, and the Coulomb parameter averaged over the last third of the run is $\bar{\Gamma}$ (determined from the final temperature and $x_{\rm O}$). The composition of the solid is x_s, of the liquid is x_l, and of the interface regions is x_i. Statistical errors are quoted in the last digit in parentheses.

$x_{\rm Se}$	$\bar{\Gamma}$	$x^s_{\rm Se}$	$x^l_{\rm Se}$	$x^i_{\rm Se}$
0.98	201.1(6)	0.9926(5)	0.966(1)	0.975(2)
0.90	213.4(8)	0.9708(7)	0.843(1)	0.884(4)
0.80	252.5(6)	0.968(1)	0.681(1)	0.762(7)
0.70	289(1)	0.970(1)	0.547(1)	0.655(4)
0.60	391(1)	0.935(2)	0.408(1)	0.513(8)
0.50	459(2)	0.902(2)	0.308(1)	0.436(9)

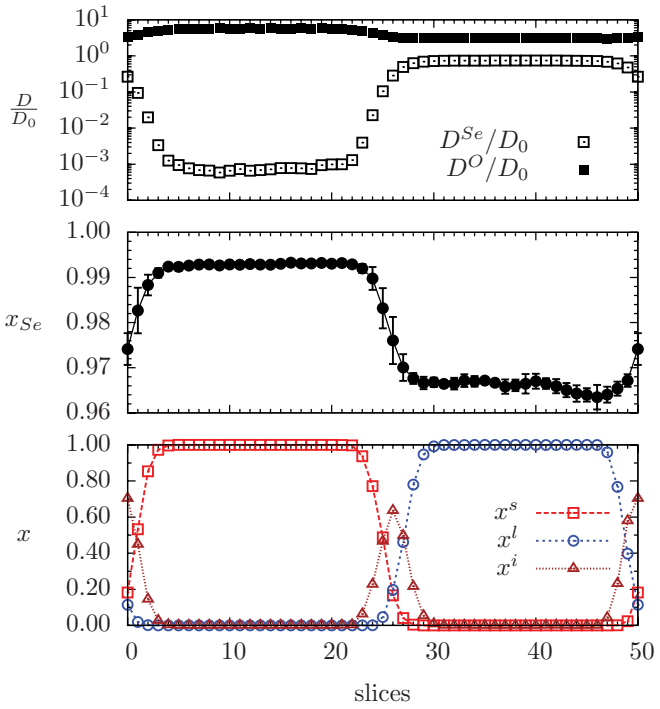

FIG. 15. (Color online) Diffusion constant D (top panel) for selenium (open squares) and oxygen ions (filled squares) for different slices (regions) of the simulation volume. Number fractions of selenium x_{Se} (middle panel) for different slices. Fractions of ions x (bottom panel) that are in the solid (squares), liquid (circles), and interface (triangles) for different slices. This is an average over the last $1.4 \times 10^5 \bar{\omega}_p t$ of a 55 296-ion simulation that is overall 2% oxygen and 98% selenium.

that the initial compositions of the 432-ion solid and 3456-ion liquid systems were set to 90% selenium. We then follow the procedure laid out in Sec. IV A to obtain a 55 296-ion configuration.

The temperature was adjusted during the run to keep approximately equal volume fractions of solid and liquid as shown in Fig. 16. The number fractions of selenium x_{Se} in the solid, liquid, and interface are shown in Fig. 17 versus simulation time. These fractions do not change much in the second half of the run, suggesting that the system is (at least approximately) equilibrated, as for the run with 98% selenium.

TABLE IV. Diffusion coefficients of liquid and solid phases averaged over the last third of the runs. Results are expressed as D_X^p in units of D_0. The letter p denotes the phase, s for solid and l for liquid, while X stands for the ion species, O for oxygen and Se for selenium. Statistical errors are quoted in the last digit in parentheses.

x_{Se}	D^l_{O}	D^l_{Se}	D^s_{O}	D^s_{Se}
0.98	3.17(1)	0.736(3)	5.66(1)	0.00080(2)
0.90	3.04(1)	0.729(2)	5.34(3)	0.00064(7)
0.80	2.88(1)	0.721(6)	4.50(9)	0.00044(7)
0.70	2.81(1)	0.771(2)	1.82(1)	0.00014(1)
0.60	2.36(1)	0.617(6)	0.18(2)	0.00002(1)
0.50	2.12(1)	0.547(2)	0.1(1)	0.00001(1)

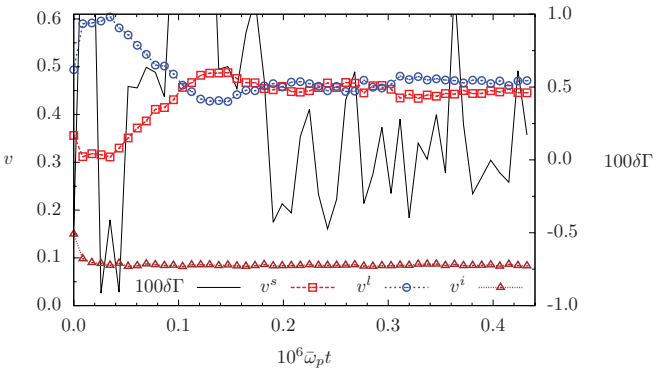

FIG. 16. (Color online) Volume fractions of solid (squares), liquid (circles), and interface (triangles) versus time for a 55 296-ion simulation that is overall 10% oxygen and 90% selenium. Also shown are fluctuations $\delta\Gamma$ in the Coulomb parameter (solid line); see Eq. (10).

In Fig. 18, in the middle panel, we show the number fraction of selenium x_{Se} for different slices (regions) of the simulation volume. This is at the end of the simulation. In the solid, x_{Se} is seen to be nearly constant and independent of position. This is consistent with the system having reached equilibration. Diffusion constants D are also shown in Fig. 18 in the top panel and are seen to behave in a similar way to Fig. 15.

C. Run with 80% selenium

The inital conditions for this simulation were prepared similarly to the initial conditions for the 98% and 90% selenium systems. However, expecting the solid to be enriched in selenium and desiring the system to reach equilibrium faster, we start the liquid and the solid subsystems with different initial compositions. We start with a 432-ion solid configuration that is 90% selenium and a 3456-liquid configuration that is 70% selenium. We then follow the procedure of Sec. IV A to obtain the 55 296-ion 80% selenium system. We note here that due to their different initial compositions, the solid and the liquid initially have different electron densities. However, the electron densities quickly equilibrate.

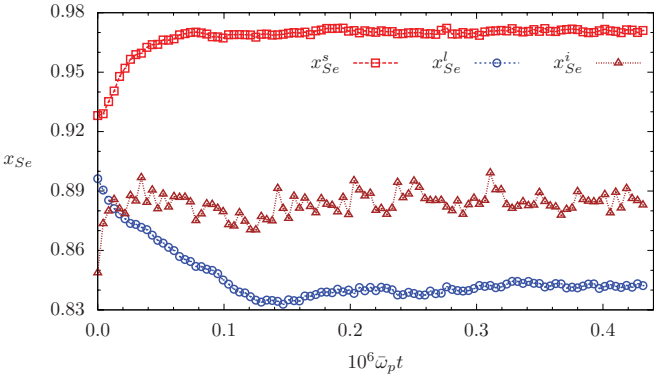

FIG. 17. (Color online) Number fractions of selenium x_{Se} in the solid (squares), liquid (circles), and interface (triangles) versus time for a 55 296-ion simulation that is overall 10% oxygen and 90% selenium.

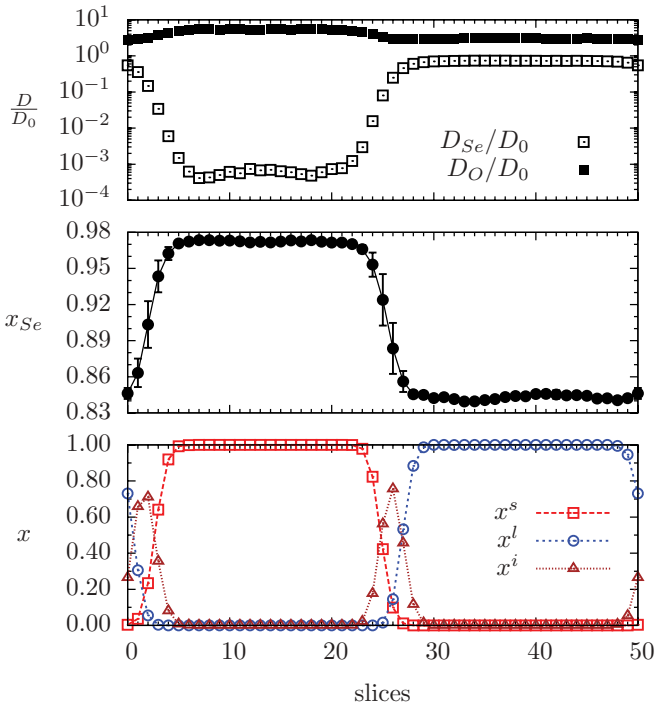

FIG. 18. (Color online) Diffusion constant D (top panel) for selenium (open squares) and oxygen ions (filled squares) for different slices (regions) of the simulation volume. Number fraction of selenium x_{Se} (middle panel) for different slices. Fractions of ions x (lower panel) that are in the solid (squares), liquid (circles), and interface (triangles) for different slices. This is an average over the last $1.4 \times 10^5 \bar{\omega}_p t$ of a 55 296-ion simulation that is overall 10% oxygen and 90% selenium.

The temperature was adjusted during the run to keep approximately equal volume fractions of solid and liquid as shown in Fig. 19. The number fractions of selenium x_{Se} in the solid, liquid, and interface are shown in Fig. 20 versus simulation time. These fractions do not change much in the second half of the run, suggesting that the system is (at least approximately) equilibrated.

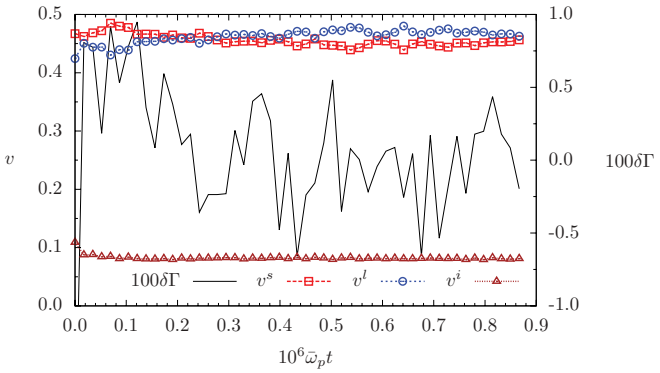

FIG. 19. (Color online) Volume fractions of solid (squares), liquid (circles), and interface (triangles) versus time for a 55 296-ion simulation that is overall 20% oxygen and 80% selenium. Also shown are fluctuations $\delta\Gamma$ in the Coulomb parameter (solid line); see Eq. (10).

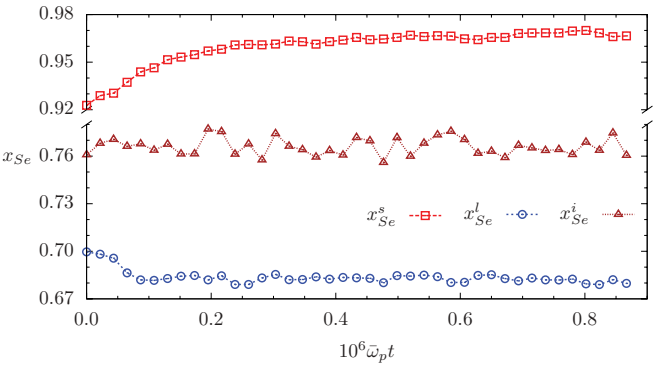

FIG. 20. (Color online) Number fractions of selenium x_{Se} in the solid (squares), liquid (circles), and interface (triangles) versus time for a 55 296-ion simulation that is overall 20% oxygen and 80% selenium.

In Fig. 21, in the middle panel, we show the number fractions of selenium x_{Se} for different slices (regions) of the simulation volume. This is at the end of the simulation. In the solid, x_{Se} is seen to be nearly constant and independent of position. This is consistent with the system having reached equilibration. Diffusion constants D are also shown in Fig. 21 in the top panel and are seen to behave in a similar way to Fig. 15.

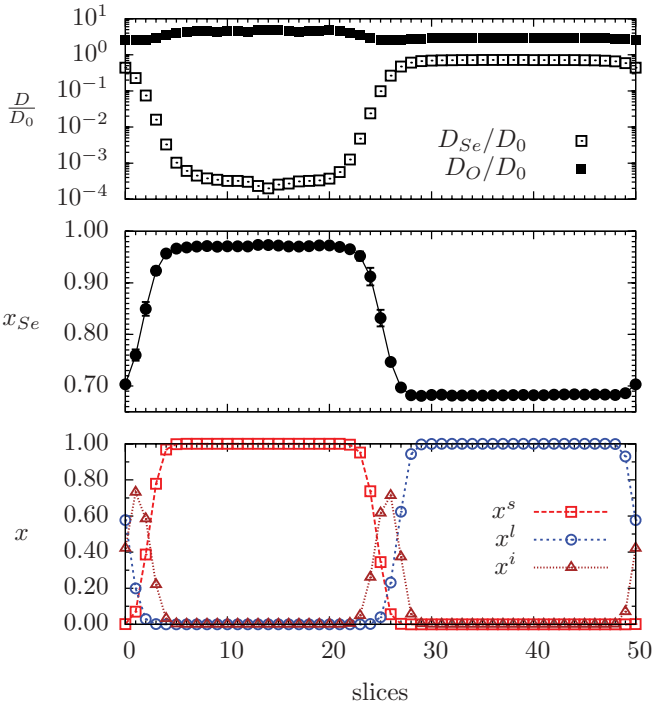

FIG. 21. (Color online) Diffusion constant D (top panel) for selenium (open squares) and oxygen ions (filled squares) for different slices (regions) of the simulation volume. Number fractions of selenium x_{Se} (middle panel) for different slices. Fractions of ions x (bottom panel) that are in the solid (squares), liquid (circles), and interface (triangles) for different slices. This is an average over the last $1.4 \times 10^5 \bar{\omega}_p t$ of a 55 296-ion simulation that is overall 20% oxygen and 80% selenium.

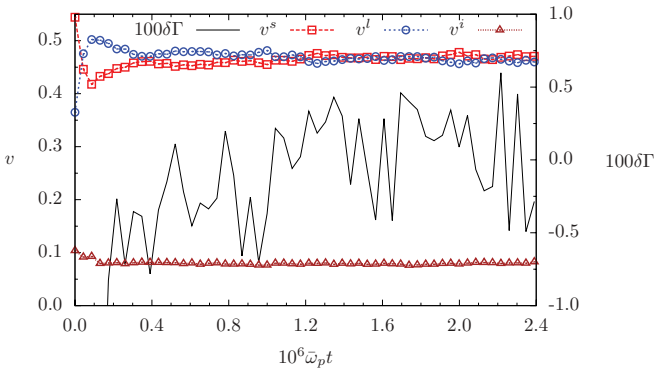

FIG. 22. (Color online) Volume fractions of solid (squares), liquid (circles), and interface (triangles) versus time for a 55 296-ion simulation that is overall 30% oxygen and 70% selenium. Also shown are fluctuations $\delta\Gamma$ in the Coulomb parameter (solid line); see Eq. (10).

D. Run with 70% selenium

The initial conditions for this simulation were prepared similarly to the initial conditions for the 80% selenium system. The initial 432-ion solid was, again, composed of 90% selenium while the 3456-ion liquid was set to 50% selenium.

The temperature was adjusted during the run to keep approximately equal volume fractions of solid and liquid as shown in Fig. 22. The number fractions of selenium x_{Se} in the solid, liquid, and interface are shown in Fig. 23 versus simulation time. The fraction of selenium in the solid may be increasing very slowly with time while x_{Se} in the liquid may be slowly decreasing. Because this change is very slow the system may be near equilibration. However, it is possible that x_{Se} could continue to change for much longer run times.

In Fig. 24, in the middle panel, we show the number fractions of selenium x_{Se} for different slices (regions) of the simulation volume. This is at the end of the simulation. In the solid, x_{Se} is seen to be nearly constant and independent of position. This is consistent with the system having reached equilibration. Diffusion constants D are also shown in Fig. 24 in the top panel and are seen to behave in a similar way to Fig. 15. However, now D for selenium is seen to change slightly with position in the solid near the interface regions.

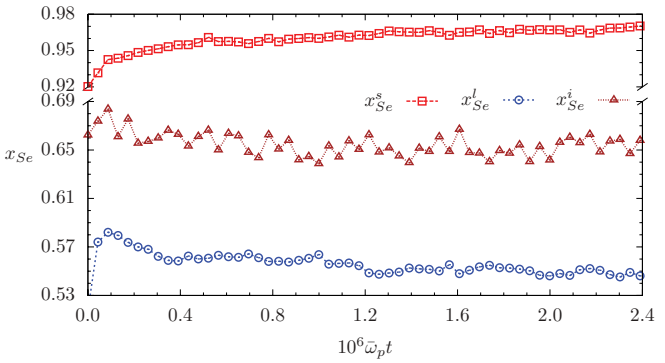

FIG. 23. (Color online) Number fractions of selenium x_{Se} in the solid (squares), liquid (circles), and interface (triangles) versus time for a 55 296-ion simulation that is overall 30% oxygen and 70% selenium.

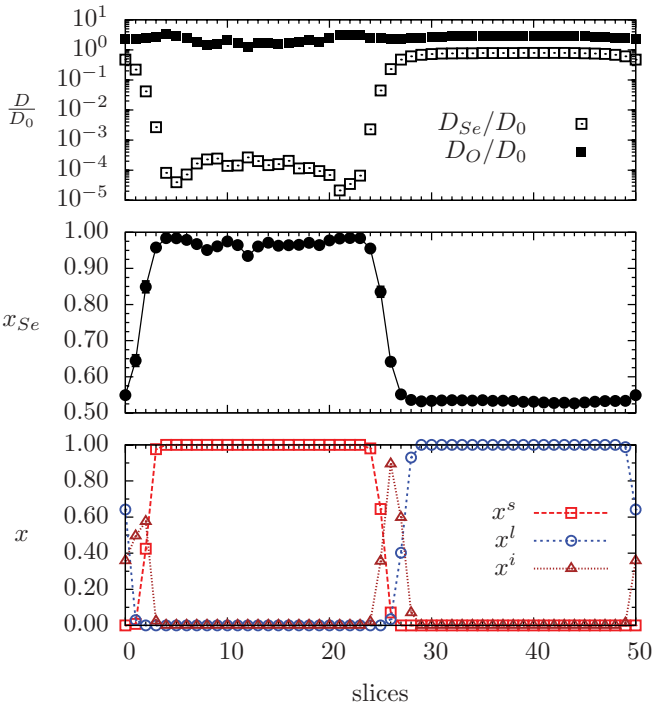

FIG. 24. (Color online) Diffusion constants D (top panel) for selenium (open squares) and oxygen ions (filled squares) for different slices (regions) of the simulation volume. Number fractions of selenium x_{Se} (middle panel) for different slices. Fraction of ions x (bottom panel) that are in the solid (squares), liquid (circles), and interface (triangles) for different slices. This is an average over the last $1.4 \times 10^5 \bar{\omega}_p t$ of a 55 296-ion simulation that is overall 30% oxygen and 70% selenium.

E. Run with 60% selenium

The initial conditions for this simulation were prepared similarly to the initial conditions for the 80% selenium system. The initial 432-ion solid was composed of 90% selenium while the 3456-ion liquid was set to 30% selenium.

The system started with a large solid fraction. The temperature was increased to bring the solid fraction approximately equal with the liquid fraction, as shown in Fig. 25. The number

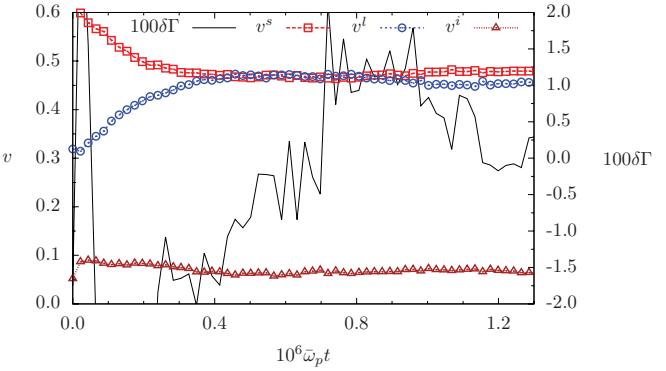

FIG. 25. (Color online) Volume fractions of solid (squares), liquid (circles), and interface (triangles) versus time for a 55 296-ion simulation that is overall 40% oxygen and 60% selenium. Also shown are fluctuations $\delta\Gamma$ in the Coulomb parameter (solid line); see Eq. (10).

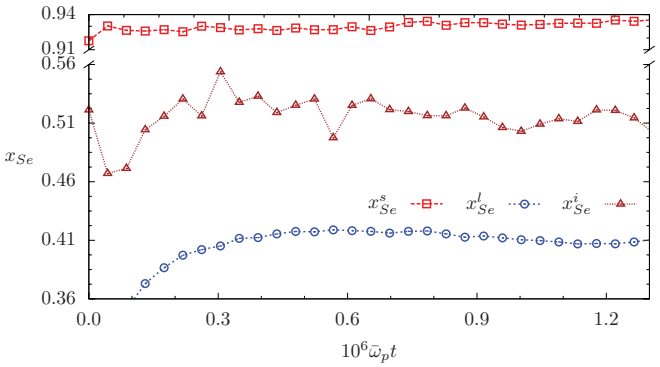

FIG. 26. (Color online) Number fractions of selenium x_{Se} in the solid (squares), liquid (circles), and interface (triangles) versus time for a 55 296-ion simulation that is overall 40% oxygen and 60% selenium.

fractions of senium x_{Se} in the solid, liquid, and interface are shown in Fig. 26 versus simulation time. Again the fraction of selenium in the solid may be increasing slightly over the second half of the run.

In Fig. 27, in the middle panel, we show the number fractions of selenium x_{Se} for different slices (regions) of the simulation volume. This is at the end of the simulation. In the solid, x_{Se} depends on position, as do the diffusion constants D as shown in the top panel of Fig. 27. This clearly indicates that

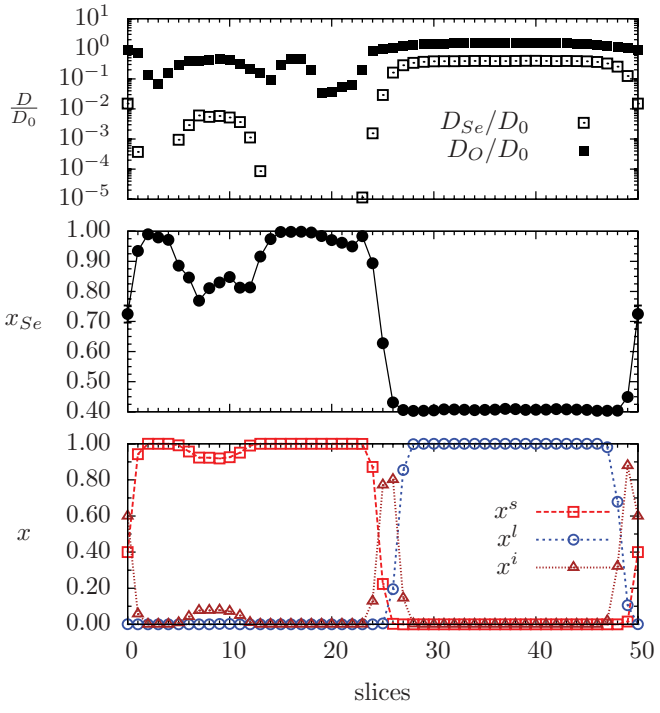

FIG. 27. (Color online) Diffusion constants D (top panel) for selenium (open squares) and oxygen ions (filled squares) for different slices (regions) of the simulation volume. Number fractions of selenium x_{Se} (middle panel) for different slices. Fractions of ions x (bottom panel) that are in the solid (squares), liquid (circles), and interface (triangles) for different slices. This is an average over the last $1.4 \times 10^5 \bar{\omega}_p t$ of a 55 296-ion simulation that is overall 40% oxygen and 60% selenium.

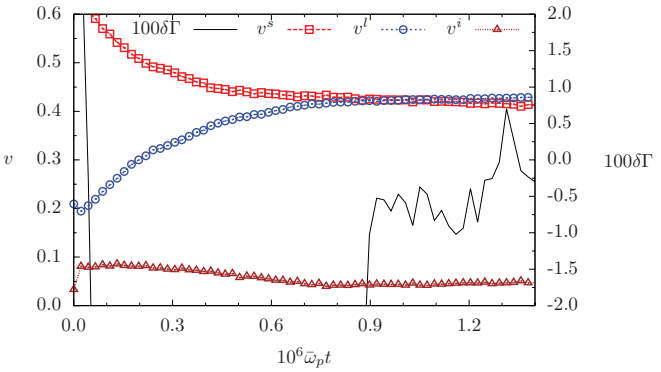

FIG. 28. (Color online) Volume fractions of solid (squares), liquid (circles), and interface (triangles) versus time for a 55 296-ion simulation that is overall 50% oxygen and 50% selenium. Also shown are fluctuations $\delta\Gamma$ in the Coulomb parameter (solid line); see Eq. (10).

the system has not reached equilibrium. Therefore we cannot use this run to determine the phase diagram in Sec. IV G. Unfortunately, the equilibration time may be very long for this composition and therefore require an unreasonable amount of simulation time in order to bring the system into equilibration.

F. Run with 50% selenium

The initial conditions for this simulation were prepared similarly to the initial conditions for the 80% selenium system. The initial 432-ion solid was, again, composed of 90% selenium while the 3456-ion liquid was set to 10% selenium.

The system started with a large solid fraction. The temperature was increased to bring the solid fraction approximately equal with the liquid fraction as shown in Fig. 28. The number fractions of selenium x_{Se} in the solid, liquid, and interface are shown in Fig. 29 versus simulation time. Now the fraction of selenium in the solid may be decreasing slightly and x_{Se} for the liquid increasing slightly with time over the second half of the run.

In Fig. 30, in the middle panel, we show the number fractions of selenium x_{Se} for different slices (regions) of the simulation volume. This is at the end of the simulation. In the

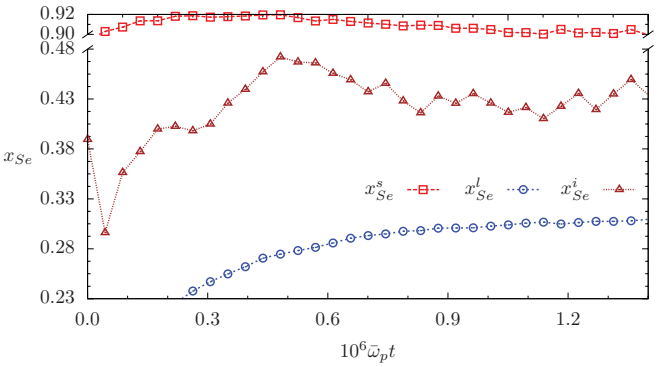

FIG. 29. (Color online) Number fractions of selenium x_{Se} in the solid (squares), liquid (circles), and interface (triangles) versus time for a 55 296-ion simulation that is overall 50% oxygen and 50% selenium.

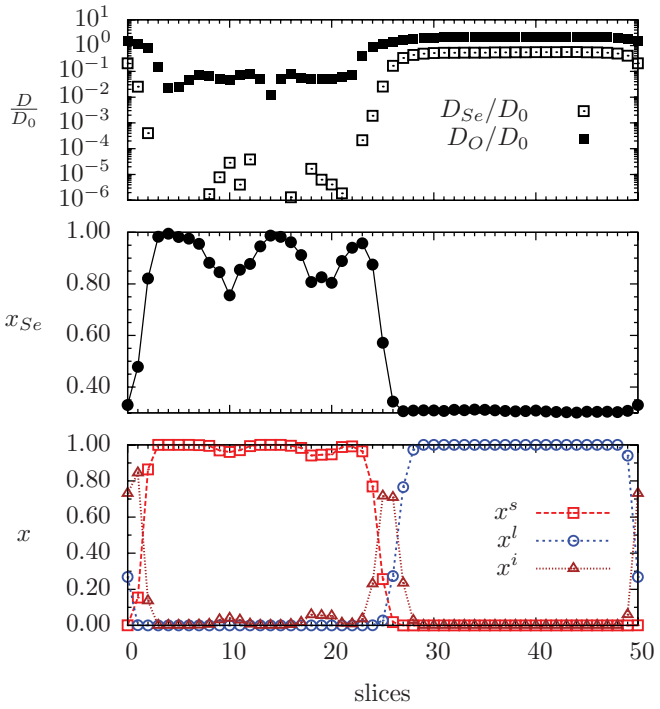

FIG. 30. (Color online) Diffusion constants D (top panel) for selenium (open squares) and oxygen ions (filled squares) for different slices (regions) of the simulation volume. Number fractions of selenium x_{Se} (middle panel) for different slices. Fractions of ions x (bottom panel) that are in the solid (squares), liquid (circles), and interface (triangles) for different slices. This is an average over the last $1.4 \times 10^5 \bar{\omega}_p t$ of a 55 296-ion simulation that is overall 50% oxygen and 50% selenium.

solid, x_{Se} depends on position, as do the diffusion constants D as shown in the top panel of Fig. 30. This is similar to the run with 60% selenium and clearly indicates that the system has not reached equilibrium. Therefore we cannot use this run to determine the phase diagram in Sec. IV G. Unfortunately, the equilibration time for this composition may also be very long and therefore require an unreasonable amount of simulation time in order to bring the system into equilibration.

G. Oxygen-selenium phase diagram

We now present the liquid-solid phase diagram implied by the simulations in Secs. IV A, IV B, IV C, IV D, IV E, and IV F. We use the data in Table III. Figure 31 shows the phase diagram as a function of x_{Se}. The y axis is the melting temperature T divided by the melting temperature T_{O} for pure oxygen. We assume that the pure oxygen system melts at $\Gamma_m = 178.4$ [26]. This differs slightly from the one-component plasma result because we include the effects of electron screening.

The filled upward-pointing triangles in Fig. 31 show the composition of the liquid phase, and the filled squares the composition of the solid phase for 55 296-ion simulations. Also shown as filled downward-pointing triangles and filled diamonds are the liquid and solid compositions for runs that are clearly not equilibrated. These points should not be used in the determination of the phase diagram. The open triangles (liquid) and squares (solid) show results for smaller

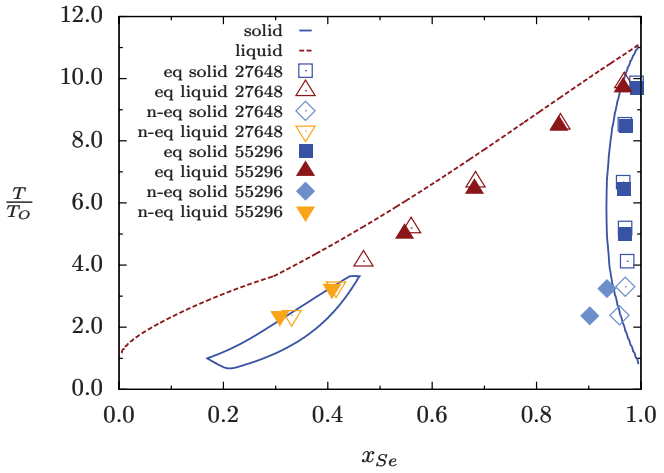

FIG. 31. (Color online) Selenium-oxygen phase diagram plotting the composition of the liquid phase (upper red curve or triangles) that is in equilibrium with the solid phase (lower blue curve or squares). Results from 55 296-ion simulations are filled symbols while the open symbols are results with 27 648 ions. Besides results discussed in the text there is an extra 27 648-ion simulation with $x_{\mathrm{Se}} = 0.65$. The curves are the results of Medin and Cumming [21].

27 648-ion simulations; see Table V. In general there is very good agreement between equilibrated 55 296- and 27 648-ion simulations. This suggests that finite-size effects, while not strictly zero, are small.

The blue solid lines in Fig. 31 show the solid composition, and the dotted brown line the liquid composition, for the phase diagram of Medin and Cumming [21]. There is qualitative agreement between these curves and our results for the $x_{\mathrm{Se}} > 0.5$ half of the phase diagram where we have apparently equilibrated independent results. However, there are some differences in detail. We find a somewhat larger selenium solid composition while our melting temperature for the liquid is somewhat lower than that of Medin and Cumming. This difference in melting temperature may be due to electron screening effects that are included in our simulations and neglected in Medin and Cumming's free energies.

Screening depends on the ratio of ion sphere radius a to screening length λ; see Eq. (1). For a very relativistic electron

TABLE V. Equilibrium compositions of 27 648-ion runs. The selenium number fraction of the whole system is x_{Se}. Note that runs with $x_{\mathrm{Se}} = 0.60$ and 0.50 are not equilibrated. The Coulomb parameter averaged over the last third of the run is $\bar{\Gamma}$. The composition of the solid is x^s_{Se}, the liquid is x^l_{Se}, and the interface regions is x^i_{Se}. Statistical errors are quoted in the last digit in parentheses.

x_{Se}	$\bar{\Gamma}$	x^s_{Se}	x^l_{Se}	x^i_{Se}
0.98	198.1(7)	0.991(1)	0.968(1)	0.976(2)
0.90	212.0(8)	0.969(2)	0.846(4)	0.888(4)
0.80	244(2)	0.966(2)	0.683(3)	0.764(6)
0.70	279(1)	0.970(2)	0.560(3)	0.650(8)
0.65	329(1)	0.973(2)	0.469(3)	0.559(6)
0.60	383(1)	0.971(2)	0.415(3)	0.487(7)
0.50	456(1)	0.959(1)	0.330(1)	0.400(6)

gas this ratio depends only on the average ion charge $\langle Z\rangle$ and is independent of density,

$$\kappa = \frac{a}{\lambda} = \left(\frac{2^{1/3}3^{2/3}}{\pi^{1/6}}\right)\alpha^{1/2}\langle Z\rangle^{1/3}. \tag{12}$$

For a one-component Yukawa system the value of Γ at the melting point, Γ_m, is [40]

$$\Gamma_m(\langle Z\rangle) \approx 171.8 + 42.46\kappa^2 + 3.841\kappa^4, \tag{13}$$

for $\kappa \leqslant 1.4$. For pure oxygen we have

$$\Gamma_m(8) = 178, \tag{14}$$

while for pure selenium,

$$\Gamma_m(34) = 188. \tag{15}$$

Thus pure selenium melts at a 6% higher Γ value than pure oxygen because of enhanced electron screening. In order to study the differences between our MD simulation results for T/T_O in Fig. 31 and Medin and Cumming's results, we rescale Medin and Cumming's melting temperatures according to

$$\frac{T}{T_O} \rightarrow \frac{\Gamma_m(8)}{\Gamma_m(\langle Z\rangle)}\frac{T}{T_O} \tag{16}$$

and plot the rescaled results in Fig. 32. This procedure ensures that the rescaled Medin and Cumming results will reproduce Eq. (14) for pure oxygen and Eq. (15) for pure selenium. In between, for a mixture of oxygen and selenium, we somewhat arbitrarily assume that the electron screening correction depends only on $\langle Z\rangle$.

There is good agreement between our MD results in Fig. 32 and these rescaled Medin and Cumming results for simulations with 90% or 98% selenium. However, for simulations with smaller $x_{\rm Se}$, our MD results give somewhat lower melting temperatures and have less oxygen in the solid phase. These differences could be due to finite-size or nonequilibrium effects in our MD simulations. However, we find only very small differences between 27 648- and 55 296-ion simulations. Furthermore, except for the low-$x_{\rm Se} = 50\%$ or 60% runs, we find very little time dependence in our simulations. Alternatively, the differences could be due to electron screening effects for mixtures that are not well described by the rescaling in Eq. (16). Finally, the differences could be due to limitations in the liquid and solid free energies used by Medin and Cumming.

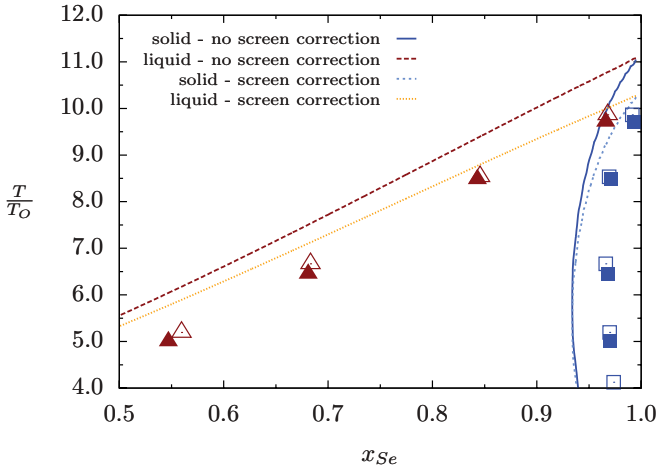

FIG. 32. (Color online) Enlargement of the large-$x_{\rm Se}$ part of the selenium-oxygen phase diagram from Fig. 31. The heavy dashed and solid lines are the results of Medin and Cumming [21], while the light dashed lines are our rescaling of Medin and Cumming's results to approximately include the effects of electron screening, as discussed in the text.

Unfortunately our simulations with 50% and 60% selenium did not reach equilibrium. Therefore we are not able to effectively study the phase diagram for low selenium concentrations. Medin and Cumming predict regions of the phase diagram with equilibria between different solid phases. Perhaps by carefully preparing initial conditions that include two solid phases of different compositions, one may be able to study solid-solid phase equilibria with our direct MD simulation procedure. However, the small diffusion constants for selenium in the solid have made it difficult for us to equilibrate the simulations with small selenium concentrations presented here. Note that this region of the phase diagram, with small $x_{\rm Se}$, may not be important in applications for neutron stars.

The complex rapid proton capture nucleosynthesis ash composition considered in Ref. [10] was predominantly selenium, with only small concentrations of oxygen and a number of other impurities. We modeled this 17-component composition with a binary system of oxygen impurities mixed with the dominant element selenium. Direct MD simulations of the full rp ash composition in Ref. [10], Table I, found the concentration of oxygen in the liquid phase to be six times larger than the oxygen concentration of the solid phase. While we find, in the first two rows of Table III, that the oxygen concentration of the liquid phase, for our simplified binary mixture simulations, is five times larger than that in the solid phase. We conclude that this binary mixture model provides a reasonable description of the freezing behavior of the rp ash.

V. SUMMARY AND CONCLUSIONS

We have determined the liquid-solid phase diagram for carbon-oxygen and oxygen-selenium plasma mixtures using two-phase MD simulations. We identified liquid, solid, and interface regions in our simulations using a bond angle metric described in Sec. II B. To study finite-size effects, we performed both 27 648- and 55 296-ion simulations. To help monitor nonequilibrium effects, we calculated diffusion constants D_i. For the carbon-oxygen system, we find that $D^s_{\rm O}$ for oxygen ions in the solid is much smaller than $D^s_{\rm C}$ for carbon ions and that both diffusion constants are 80 or more times smaller than diffusion constants in the liquid phase. There is excellent agreement between our carbon-oxygen phase diagram and that predicted by Medin and Cumming [21]. This suggests that errors from finite-size and nonequilibrium effects are small, and that the carbon-oxygen phase diagram may be accurately known.

The oxygen-selenium system, with a larger ratio of charges than the carbon-oxygen mixture, can serve as a simple two-component model of the complex rapid proton capture ash composition on an accreting neutron star. We find that diffusion

of oxygen in a predominantly selenium crystal is remarkably fast and is comparable to diffusion in the liquid phase. Our MD simulations have a somewhat lower melting temperature for the oxygen-selenium system than that predicted by Medin and Cumming. This is in part due to electron screening effects, which are included in our simulations and may be neglected by Medin and Cumming. In the future, we will present MD simulations of the phase diagram for the three-component carbon-oxygen-neon system to include the effects of neon impurities in carbon-oxygen white dwarfs. In addition, we will describe the structure of the carbon-oxygen and oxygen-selenium Coulomb crystals.

ACKNOWLEDGMENTS

We thank Z. Medin for helpful discussions. This research was supported in part by DOE Grant No. DE-FG02-87ER40365 and by the National Science Foundation through TeraGrid resources provided by the National Institute for Computational Sciences under Grant No. TG-AST100014.

[1] G. Fontaine, P. Brassard, and P. Bergeron, Publ. Astron. Soc. Pac. **113**, 409 (2001).
[2] E. Garcia-Berro, S. Torres, I. Renedo, J. Camacho, L. G. Althaus, A. H. Corsico, M. Salaris, and J. Isern, Astron. Astrophys. **533**, A31 (2011).
[3] I. Renedo, L. G. Althaus, M. M. Miller Bertolami, A. D. Romero, A. H. Corsico, R. D. Rohrmann, and E. Garca-Berro, Astrophys. J. **717**, 183 (2010).
[4] M. Salaris, S. Cassisi, A. Pietrinferni, P. M. Kowalski, and J. Isern, Astrophys. J. **716**, 1241 (2010).
[5] M. Salaris, I. Domnguez, E. Garca-Berro, M. Hernanz, J. Isern, and R. Mochkovitch, Astrophys. J. **486**, 413 (1997).
[6] D. E. Winget *et al*., Astrophys. J. **693**, L6 (2009).
[7] T. S. Metcalfe, Mon. Not. R. Astron. Soc. **363**, L86 (2005).
[8] H. Schatz, A. Aprahamian, V. Barnard, L. Bildsten, A. Cumming, M. Ouellette, T. Rauscher, F. K. Thielemann, and M. Wiescher, Phys. Rev. Lett. **86**, 3471 (2001).
[9] S. E. Woosley, A. Hager, A. Cumming, R. D. Hoffman, J. Pruet, T. Rauscher, J. L. Fisker, H. Schatz, B. A. Brown, and M. Wiescher, Astrophys. J. Suppl. Ser. **151**, 75 (2004).
[10] C. J. Horowitz, D. K. Berry, and E. F. Brown, Phys. Rev. E **75**, 066101 (2007).
[11] A. Cumming and L. Bildsten, Astrophys. J. **559**, L127 (2001).
[12] T. E. Strohmayer and E. F. Brown, Astrophys. J. **566**, 1045 (2002).
[13] A. Cumming, J. Macbeth, J. J. M. in 't Zand, and D. Page, Astrophys. J. **646**, 429 (2006).
[14] L. Segretain and G. Chabrier, Astron. Astrophys. **271**, L13 (1993).
[15] S. Ogata, H. Iyetomi, S. Ichimaru, and H. M. VanHorn, Phys. Rev. E **48**, 1344 (1993).
[16] S. Ichimaru, H. Iyetomi, and S. Ogata, Astrophys. J. **334**, L17 (1988).
[17] H. DeWitt and W. Slattery, Contrib. Plasma Phys. **43**, 279 (2003).
[18] H. DeWitt, W. Slattery, and G. Chabrier, Physica B **228**, 21 (1996).
[19] A. Y. Potekhin, G. Chabrier, and F. J. Rogers, Phys. Rev. E **79**, 016411 (2009).
[20] A. Y. Potekhin, G. Chabrier, A. I. Chugunov, H. E. DeWitt, and F. J. Rogers, Phys. Rev. E **80**, 047401 (2009).
[21] Z. Medin and A. Cumming, Phys. Rev. E **81**, 036107 (2010).
[22] R. L. Cooper and L. Bildsten, Phys. Rev. E **77**, 056405 (2008).
[23] J. Daligault, Phys. Rev. E **73**, 056407 (2006).
[24] H. Totsuji, J. Phys. C **19**, L573 (1986).
[25] I. Iosilevski and A. Chigvintsev, in *Strongly Coupled Coulomb Systems*, edited by C. Deutsch, B. Jankovici, and M.-M. Gombert, special issue of J. de Physique IV **10**, Pr5-451 (2000).
[26] C. J. Horowitz, A. S. Schneider, and D. K. Berry, Phys. Rev. Lett. **104**, 231101 (2010).
[27] J. Hughto, A. S. Schneider, C. J. Horowitz, and D. K. Berry, Phys. Rev. E **84**, 016401 (2011).
[28] V. E. Fortov, A. V. Ivlev, S. A. Khrapak, A. G. Khrapak, and G. E. Morfill, Phys. Rep. **421**, 1 (2005).
[29] H. Thomas, G. E. Morfill, V. Demmel, J. Goree, B. Feuerbacher, and D. Mohlmann, Phys. Rev. Lett. **73**, 652 (1994).
[30] S. A. Khrapak *et al*., Phys. Rev. Lett. **106**, 205001 (2011).
[31] N. J. Lorenz and T. Palberg, J. Chem. Phys. **133**, 104501 (2010).
[32] A. Y. Potekhin and G. Chabrier, Phys. Rev. E**62**, 8554 (2000).
[33] A. Y. Potekhin, D.Sc. thesis, http://www.ioffe.ru/astro/DTA/palex/disser.pdf, [Contrib. Plasma Phys. (to be published)] (in Russian).
[34] M. D. Jones and D. M. Ceperley, Phys. Rev. Lett. **76**, 4572 (1996).
[35] P. J. Steinhardt, D. R. Nelson, and M. Ronchetti, Phys. Rev. B **28**, 784 (1983).
[36] P. R. ten Wolde, M. J. Ruiz-Montero, and D. Frankel, J. Chem. Phys. **104**, 9932 (1996).
[37] L. Verlet, Phys. Rev. **159**, 98 (1967).
[38] National Institute for Computational Sciences, U. Tenn. and Oak Ridge National Laboratory.
[39] J. Hughto, A. S. Schneider, C. J. Horowitz, and D. K. Berry, Phys. Rev. E **82**, 066401 (2010).
[40] S. Hamaguchi, R. T. Farouki, and D. H. E. Dubin, J. Chem. Phys. **105**, 7641 (1996).